Journal of ELECTRONIC MATERIALS, Vol. 49, No. 5, 2020
https://doi.org/10.1007/s11664-019-07745-y

TOPICAL COLLECTION: INTERNATIONAL CONFERENCE ON THERMOELECTRICS 2019

Preparation and Characterization of Ni/$Bi_{0.5}Sb_{1.5}Te_3$ Heterogeneous Multilayered Thermoelectric Materials

XINGE GUO,[1] WANTING ZHU,[1,2] LIN XING,[1] XIN MU,[1] CUNCHENG LI,[1] SHIFANG MA,[1] PING WEI,[1] XIAOLEI NIE,[1] QINGJIE ZHANG,[1] and WENYU ZHAO[1,3]

1.—State Key Laboratory of Advanced Technology for Materials Synthesis and Processing, Wuhan University of Technology, Wuhan 430070, China. 2.—e-mail: zwanting@whut.edu.cn. 3.—e-mail: wyzhao@whut.edu.cn

It is difficult to achieve coordinated optimization in thermoelectric materials due to the strong coupling between the electrical and thermal transport properties. However, interface effects, especially those caused by heterogeneous interfaces, are promising to overcome this challenge. In this work, the Ni/$Bi_{0.5}Sb_{1.5}Te_3$ (BST) heterogeneous multilayer structure thermoelectric materials were fabricated by the combination of vacuum evaporation deposition and spark plasma sintering. The influence of Ni layer on the phase composition, microstructure and thermoelectric performance along the different directions (0°, 30°, 60° and 90°, the angles between the performance measurement direction and the Ni layer) of Ni/BST materials were systematically investigated. The microstructural analysis indicates that the distinct heterogeneous interfaces were firmly bonded, and the interface reaction layer was composed of Ni and Te. As compared with the matrix, the electrical conductivity and Seebeck coefficient of the Ni/BST heterogeneous multilayer thermoelectric materials increased, and the thermal conductivity slightly reduced. For Ni/BST90° sample, the maximum ZT value of 1.05 was achieved at 370 K, increased by 19.1% compared with the BST90°. Our work demonstrates that the electron and phonon transport properties can be simultaneously optimized by introducing the ordered heterogeneous interfaces.

Key words: Ni, $Bi_{0.5}Sb_{1.5}Te_3$, multilayered , heterogeneous interface

INTRODUCTION

Thermoelectric (TE) materials, which realize direct energy conversion between electricity and heat by the movement of carriers (electrons and holes) in solids, have been widely used in the field of TE power generation and portable refrigeration.[1–3] The conversion efficiency of TE materials is determined by the dimensionless figure of merit, $ZT = \alpha^2\sigma T/\kappa$, where T is the absolute temperature, α is the Seebeck coefficient, σ is the electrical conductivity, and κ is the total thermal conductivity ($\kappa = \kappa_E + \kappa_L$, κ_E and κ_L are the electronic and lattice thermal conductivity, respectively). Clearly, in order to obtain a high ZT, the TE material must have high α, high σ and low κ. This turns out to be rather difficult, since all these parameters are intimately associated with each other, making it hard to regulate them individually. For example, while high σ requires high concentration of charge carriers (n), high n in turn decreases α. Furthermore, high σ is usually accompanied by high κ_E according to Wiedemann–Franz Law.[4] Therefore, it is a huge challenge to achieve high α, high σ and low κ simultaneously in a single-phase material. To optimize the thermal transport properties, various

(Received July 24, 2019; accepted October 17, 2019; published online November 6, 2019)

phonon engineering approaches have been used to enhance phonon scattering and decrease $\kappa_{L.}$[5–8] To optimize the electrical transport properties, a series of band structure engineering approaches have been developed to increase $\alpha^2\sigma$.[9–13] These methods have played important roles in controlling electron and phonon transport and improving the ZT of bulk TE materials.

The Bi_2Te_3-based alloy is the best and only commercial TE material near room temperature.[14] Bi_2Te_3 belongs to the hexagonal crystal system, and the space group is $R\bar{3}m$, which has a layered crystal structure. Its layered structure is composed of five monatomic layers alternately stacked in the order of Te^1-Bi-Te^2-Bi-Te^1, and every five layers are combined by van der Waals force. Bi-Te^2 and Bi-Te^1 are mainly bonded by covalent bonds and ionic bonds.[15] Such a layered crystal structure leads to strong anisotropy of σ and κ.[16–22] Caillat et al.[16] successfully prepared p-type $Bi_{0.5}Sb_{1.5}Te_3$ single crystals by traveling heater method (THM), and its anisotropy ratios range was from 3.0 to 4.0 in the σ, and from 2.0 to 2.5 in the κ along the parallel and perpendicular to the crystal growth direction. In addition, the polycrystals sintered by spark plasma sintering (SPS) also exhibited an anisotropic of electrical and thermal transport properties.[17,18,21] Shen et al.[17] studied the anisotropy of TE performance in Bi_2Te_3-based polycrystalline alloys. The results shown that the σ ratios of p-type and n-type along the perpendicular and parallel to the sintering pressure were 73% and 58%, respectively, and the κ ratios were 80% and 66%, respectively. During the past decade, it was expected that ZT could be enhanced by using interfacial phonon scattering to reduce κ, interfacial quantum confinement effect and carrier scattering effect to increase power factor (PF).[23–25] However, up to now, effectively controlling the order of interfaces has always been a huge challenge.

Inspired by these, we propose to regulate the TE performance of materials by introducing ordered heterointerfaces in $Bi_{0.5}Sb_{1.5}Te_3$ (BST) matrix. Ni is commonly used as a diffusion-barrier material between the electrode and the substrate in the Bi_2Te_3-based TE devices. Ni can both improve the bonding strength between solder and substrate and block the diffusion of solder to the substrate.[26–30] In addition, the interfacial products formed by Ni and Bi_2Te_3-based TE materials are mostly binary Ni_xTe_y intermetallic compounds (such as NiTe,[31,32] $NiTe_2$,[32,33] Ni_3Te_2[32]), which exhibit metal or semimetal properties[31–33] with a good electrical transport properties. On this basis, we deposit Ni films on BST wafers by vacuum evaporation then stack the BST wafer with Ni film layer by layer and obtain Ni/BST heterogeneous multilayered TE materials by SPS. In order to explore the influence of heterointerface on TE performance, the phase composition and microstructure of heterogeneous interface have been systematically studied. The results show that the σ of Ni/BST heterogeneous multilayered TE materials increases, the κ decreases and the α increases compared with the matrix. Our work demonstrates that the electron and phonon transport properties can be simultaneously optimized by introducing ordered heterogeneous interfaces.

EXPERIMENTAL PROCEDURES

The preparation procedure of Ni/$Bi_{0.5}Sb_{1.5}Te_3$ (BST) heterogeneous multilayered TE materials is as follows: Firstly, commercial zone-melted BST was pulverized, ground, and passed through a 120 mesh sieve to obtain homogeneous BST powder. Then the obtained powder was placed into 15-mm-diameter graphite die and subjected to SPS-I (723 K and 50 MPa) to get a dense polycrystalline BST cylinder. Secondly, the polycrystalline BST cylinder was cut into wafers by wire electrical discharge machining (WEDM, Chenyang CNC Machinery), then the wafers the oxide layer was polished out. Theoretically, the smaller the thickness of the BST wafer, the greater the influence on the performance of the final samples, but it is actually limited by the processing conditions, so we finally choose the 1-mm-thickness BST wafer. Thirdly, the BST wafers were placed into a vacuum evaporation deposition instrument sustaining a 4.0×10^{-3} Pa pressure to obtain the Ni/BST wafers with a layer of 180 nm Ni film. The thickness of the films was monitored by a digital quartz oscillating thickness monitor. Before evaporation deposition, the BTS wafers were first cleaned with ethanol and plasma cleaner in order to remove contaminates and improve surface chemical activity. During the evaporation process, BST wafers were rotated at a rate of 150 r/min. Finally, Ni/BST heterogeneous multilayered TE materials were successfully prepared by stacking the Ni/BST wafers into 15-mm-diameter graphite die and subjected to SPS-II (723 K and 50 MPa). It is worth noting that all BST matrixes were also prepared by the same two-step SPS. The Ni/BST heterogeneous multilayer structure TE materials were cut into the standard shape along different directions (0°, 30°, 60° and 90°, the angles between the performance measurement direction and the Ni layer) by WEDM, which was used to measure the TE performance. The electrical and thermal transport properties were measured in the same direction. The cutting diagram is shown in Fig. 1.

The phase composition of heterogeneous multilayered TE materials was determined by x-ray diffraction (XRD, Bruker D8-Advance) using Cu Kα radiation (λ = 0.15418 nm). The chemical compositions and interface were analyzed by electron probe microanalysis (EPMA, JEOL JXA-8230). The microstructures were examined by a field emission scanning electron microscope (FESEM, Hitachi-SU8020). The Hall coefficient (R_H) was measured at room temperature by van der Pauw method using a thermoelectric and magnetic performance testing

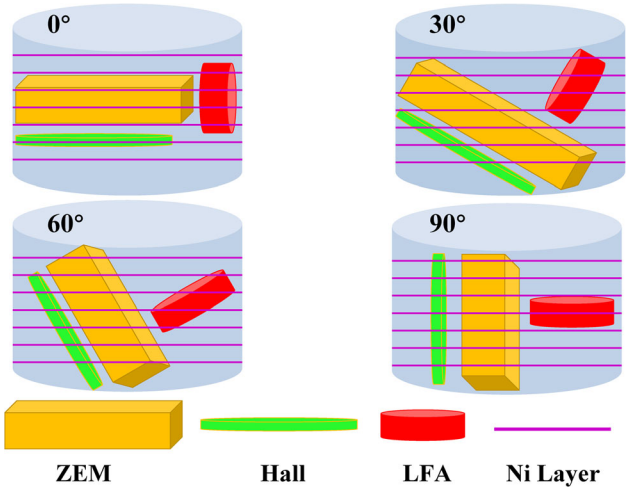

Fig. 1. Cutting diagram of Ni/BST heterogeneous multilayer structure TE material.

system (NYMS-1). The electrical conductivity (σ) and Seebeck coefficient (α) were measured using the standard four-probe method (Ulvac Riko, ZEM-3). The carrier concentration (n) and mobility (μ) were calculated using the formula $n = 1/(R_H e)$ and $\mu = R_H\sigma$, where e is the charge of an electron. The thermal conductivity (κ) was calculated by using the equation $\kappa = \lambda\rho C_p$, where C_p is the specific heat capacity, ρ is the density of materials, and λ is the thermal diffusivity coefficient. λ was measured by laser-flash technique (Netzsch LFA-427) in a flowing argon atmosphere. C_p was measured using a Q20 differential scanning calorimeter. ρ was measured by the Archimedes method. κ_L was obtained by subtracting κ_E from κ using the equation $\kappa_L = \kappa - \kappa_E$. Here, κ_E was calculated by the Wiedemann–Franz law $\kappa_E = L\sigma T$, where L is the Lorenz number and can be estimated by Seebeck coefficient $L = 1.5 + \exp\left[-\frac{|S|}{116}\right]$ [34] σ, α, and κ were measured in the temperature range from 300 K to 500 K. Uncertainties in σ and κ were ± 5 to 7%. Uncertainty in α was ± 5%.

RESULTS AND DISCUSSION

The XRD patterns of as-prepared Ni/BST heterogeneous multilayered TE materials are shown in Fig. 2. All diffraction peaks can be indexed based on JCPDS 49-1713 of $Bi_{0.5}Sb_{1.5}Te_3$. The diffraction peaks of Ni are not detected since the thickness of the Ni film is less than 200 nm and its content is about 0.05%, which exceeds the XRD detection limit.

In addition, it can be seen that the preferred orientation of Ni/BST heterogeneous multilayered TE materials is closely related to the angle. As shown in Fig. 2, the diffraction intensity of (000l) decreases gradually with the increase of the angle. To further investigate the evolution feature of preferential orientations, the orientation factors

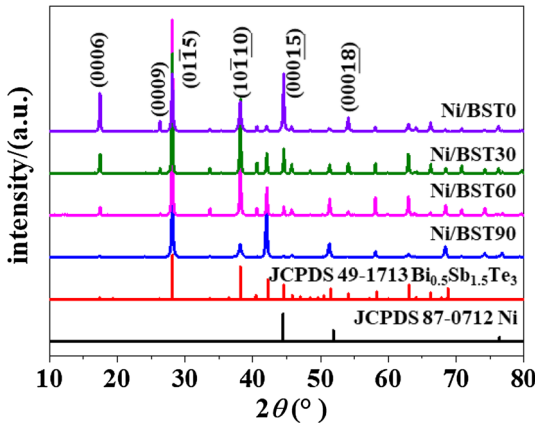

Fig. 2. XRD pattern of Ni/BST heterogeneous multilayered TE materials with different angles.

Table I. The orientation factors of Ni/BST heterogeneous multilayered TE materials with different angles

Samples	F (000l)	F(01$\bar{1}$5)	F(10$\bar{1}$10)
Ni/BST0°	0.31	− 0.16	− 0.02
Ni/BST30°	0.04	− 0.04	0.05
Ni/BST60°	− 0.08	0.15	0.01
Ni/BST90°	− 0.02	− 0.06	− 0.13

(F) were quantitatively calculated by Lotgering's method[35]:

$$F(X) = (P - P_0)/(1 - P_0) \quad (1)$$

$$P = \sum I(X)/\sum I(hkil) \quad (2)$$

$$P_0 = \sum I_0(X)/\sum I_0(hkil) \quad (3)$$

where $\sum I(X)$, $\sum I_0(X)$, $\sum I(hkil)$, and $\sum I_0(hkil)$ are the sum of the integrated intensities of the X and ($hkil$) reflections for the as-prepared Ni/BST samples and the standard diffraction card, respectively; P and P_0 are the ratio of the sums for a certain orientation of the as-prepared Ni/BST sample and the standard diffraction card, respectively. The X represents the diffraction surface of (000l), (01$\bar{1}$5), and (10$\bar{1}$10), respectively. The F values of Ni/BST heterogeneous multilayer structure TE materials with different angles are listed in Table I. As the increase of angles, the F value of (000l) decreases, and the maximum F value 0.31 is obtained in the Ni/BST0°; the F value of (01$\bar{1}$5) increases first and then decreases, and the maximum F value 0.15 is acquired in the Ni/BST60°; the F value of (10$\bar{1}$10) increases first and then decreases, and the maximum F value 0.05 is reached in the Ni/BST30°. These are consistent with the corresponding XRD diffraction peak intensity in Fig. 2.

The FESEM cross-sectional morphology of the Ni/BST heterogeneous multilayer structure TE material is displayed in Fig. 3a. The orientation characteristic of the BST matrix can be clearly observed. Apparently, the distinct heterogeneous interfaces are firmly bonded and the thickness of the interface reaction layer is about 1.5 μm. Figure 3b shows the FESEM cross-section morphology of Ni film deposited on the glass substrate under the same vapor deposition conditions, with a thickness about 180 nm.

The backscattered electron image (BEI), element distribution maps and line profiles of the cross-sections of Ni/BST heterogeneous multilayered TE materials are exhibited in Fig. 4. The distinct heterogeneous interface can be observed in BEI. The region with larger contrasts can be proved to be interfacial reaction layer composed of Ni and Te by element distribution maps and line profiles. Previous studies indicate that Ni_xTe_y compounds exhibit conduction properties of metal or semi-metal and have good electrical transport properties.[31–33]

The room-temperature electrical transport properties of Ni/BST heterogeneous multilayered TE materials with different angles are given in Table - II. The positive Hall coefficient (R_H) indicates that the majority of the carriers are holes, which displays a p-type conduction behavior. Because the Ni/BST sample have more heterogeneous interfaces and grain boundaries as the angle increases, the carrier transport is hindered causing a larger Hall voltage on both sides of the sample, resulting in an increase in Hall coefficient and a decrease in carrier concentration according to the Eqs. 4 and 5. In addition, the formed Ni-Te heterogeneous interface exhibits metal properties,[31–33] forming p-n junctions with BST matrix, neutralizing some holes, resulting in a decrease in carrier concentration.

$$R_H = V_H d / I_x B_z \tag{4}$$

$$n = 1/R_H e \tag{5}$$

where R_H is the Hall coefficient, V_H is the Hall voltage, I_x is the applied current, B_z is the applied magnetic field, d is the sample thickness, e is the charge of an electron, n is the carrier concentration. The R_H of Ni/BST0° reduces compared with BST0°, while the n and μ_H augment. This is attributed to the formation of a connected heterogeneous interface with excellent electrical transport properties,[31–33] acting as a carrier transport channel. The R_H of Ni/BST90° decreases compared with BST90°, and the n decreases slightly, while the μ_H increases. This owe to the formation of the potential barrier of heterogeneous interfaces, which filters the low-energy carriers and causes a decrease in n and an increase in μ_H, resulting in an enhancement of electrical transport properties finally. Therefore, the introduction of the ordered heterogeneous interfaces in the BST matrix can effectively regulate the electrical transport properties. The temperature dependence of electrical conductivity (σ), Seebeck coefficient (α), and power factor (PF) of Ni/BST heterogeneous multilayered TE materials with different angles are plotted in Fig. 5. The σ decreases with the increase of the measuring temperature, exhibiting a typical metal-like conduction behavior. Since the intensification of lattice vibration with increasing temperature enhances the scattering effect on carriers, resulting in a sharp decline in μ_H. Because of the intrinsic excitation, the n increases sharply after 350 K, making the decline trend of σ slow down. Moreover, the σ of the Ni/BST heterogeneous multilayer structure TE material decreases as the angle increases, which is related to the change in n and μ_H, according to the formula $\sigma = ne\mu_H$. The introduction of the Ni layer forms a heterogeneous interface with good electrical transport properties,[31–33] acting as a carrier transport channel, which explains why the σ of Ni/BST0° increases compared to the BST0° matrix. As shown in Fig. 5b, the positive values of α are indicative of p-type conduction behavior, which is consistent with the Hall coefficient measurement results.

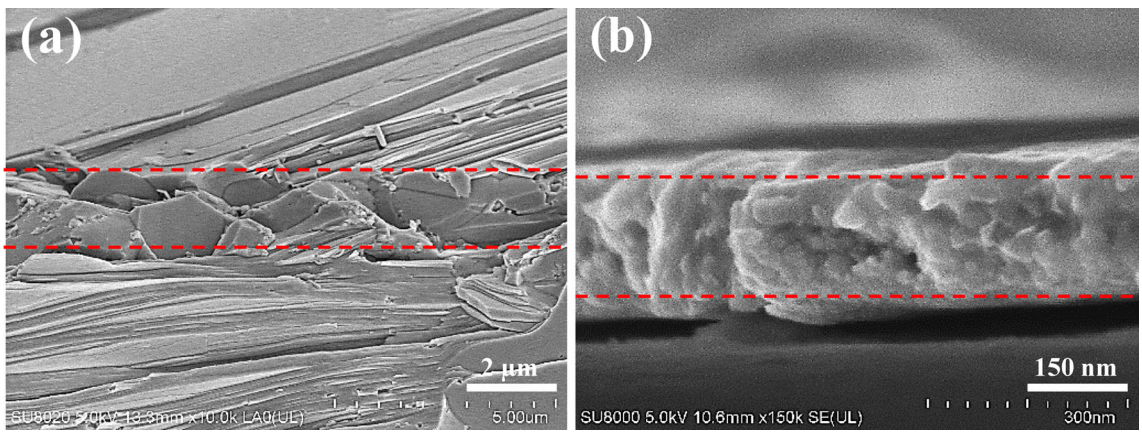

Fig. 3. (a) FESEM cross-section morphology of the Ni/BST heterogeneous multilayered TE materials and (b) the deposited Ni film.

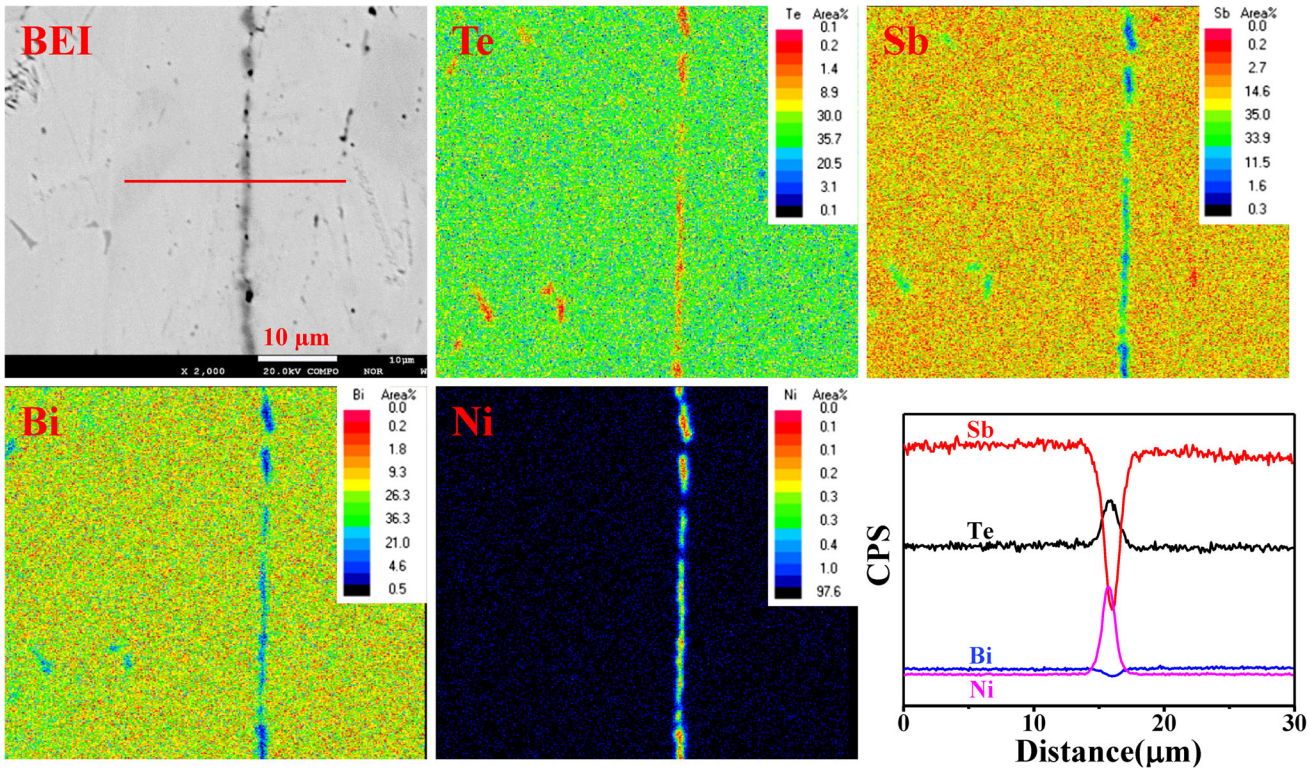

Fig. 4. BEI image, element maps distribution and line profiles of the cross-section of Ni/BST heterogeneous multilayered TE materials.

Table II. The room-temperature electrical transport properties of Ni/BST heterogeneous multilayered TE materials with different angles

Samples	R_H (10^{-1} cm^3 C^{-1})	n (10^{19} cm^{-3})	μ_H (cm^2 V^{-1} s^{-1})	σ (10^4 S m^{-1})
BST0°	3.05	2.05	260	8.53
BST90°	4.23	1.48	221	5.24
Ni/BST0°	2.82	2.22	267	9.47
Ni/BST30°	3.51	1.78	251	7.17
Ni/BST60°	3.82	1.64	245	6.43
Ni/BST90°	4.10	1.45	233	5.43

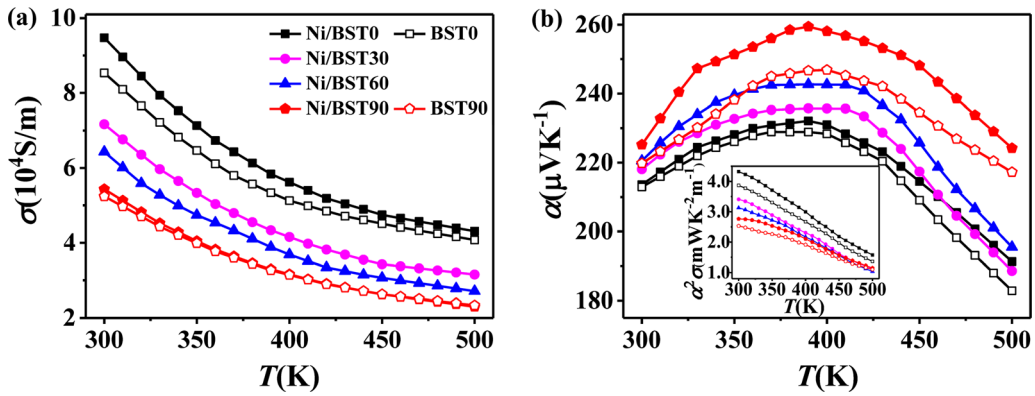

Fig. 5. Temperature dependence of (a) electrical conductivity and (b) Seebeck coefficient for Ni/BST heterogeneous multilayered TE materials with different angles. Inset in Fig. (b) shows the temperature dependence of the power factor.

Throughout the temperature range, all the samples showed similar temperature dependence of α, first ascending then descending with increasing temperature. The rapid decrease of α at high temperature is due to the intrinsic excitation of the material. With the increase of angle, the change in material anisotropy affects n, which ultimately leads to a gradual increase in α of the Ni/BST heterogeneous multilayered TE material. Particularly, the α of Ni/BST90° increases significantly compared with the BST90°, which originates from the formation of the potential barrier of heterogeneous interfaces to enhance the scattering on the carriers and filter the low-energy carriers. It can be seen from the inset of Fig. 5b that the *PF* of Ni/BST0° and Ni/BST90° increases compared with the corresponding matrix, wherein the increase of Ni/BST0° is mainly attributed to the enhancement of σ, and the increase of Ni/BST90° is due to the enhancement of α. Accordingly, the introduction of the ordered heterogeneous interface in the BST matrix can regulate its electrical transport properties by different approaches.

Figure 6 displays the temperature dependence of (a) thermal conductivity (κ), (b) electronic thermal conductivity (κ_E), (c) lattice thermal conductivity (κ_L) and (d) *ZT* values for Ni/BST heterogeneous multilayered TE materials with different angles. The κ of all samples descends first and then ascends as the temperature rises, which is determined by both κ_E and κ_L. κ_E first decreases rapidly and then tends to slow, which is consistent with the trend of σ. κ_L exhibits a tendency to decrease slightly and then increase drastically, which is determined by both the phonon scattering and the intrinsic excitation. Below the intrinsic excitation temperature, the enhancement of lattice vibration with increasing temperature enhances the phonon scattering, resulting in a decrease in κ_L. Above the intrinsic excitation temperature, the intrinsic excitation is evoked to generate a large number of electron–hole pairs, that is bipolar diffusion effect, resulting in a sharp increase in κ_L. With the increase of angle, κ_E and κ_L of Ni/BST heterogeneous multilayered TE materials decrease, eventually resulting in a decrease in κ. This originates from the preferential orientation of grains in the SPS process driven by uniaxial pressure lead to the anisotropy of the material, as reported before.[18] Because Ni/BST90° has more grain boundaries and heterogeneous interfaces, κ decreases compared with that in Ni/BST0°. The κ of Ni/BST0° increases slightly compared with that of BST0°, which is caused by the formation of connected heterogeneous interfaces. The κ of Ni/BST90° decreases compared with that of BST90°, which is attributed to the formed heterointerfaces to enhance phonon scattering. Hence, the introduction of the ordered heterogeneous interface in the BST matrix can effectively regulate its thermal transport properties.

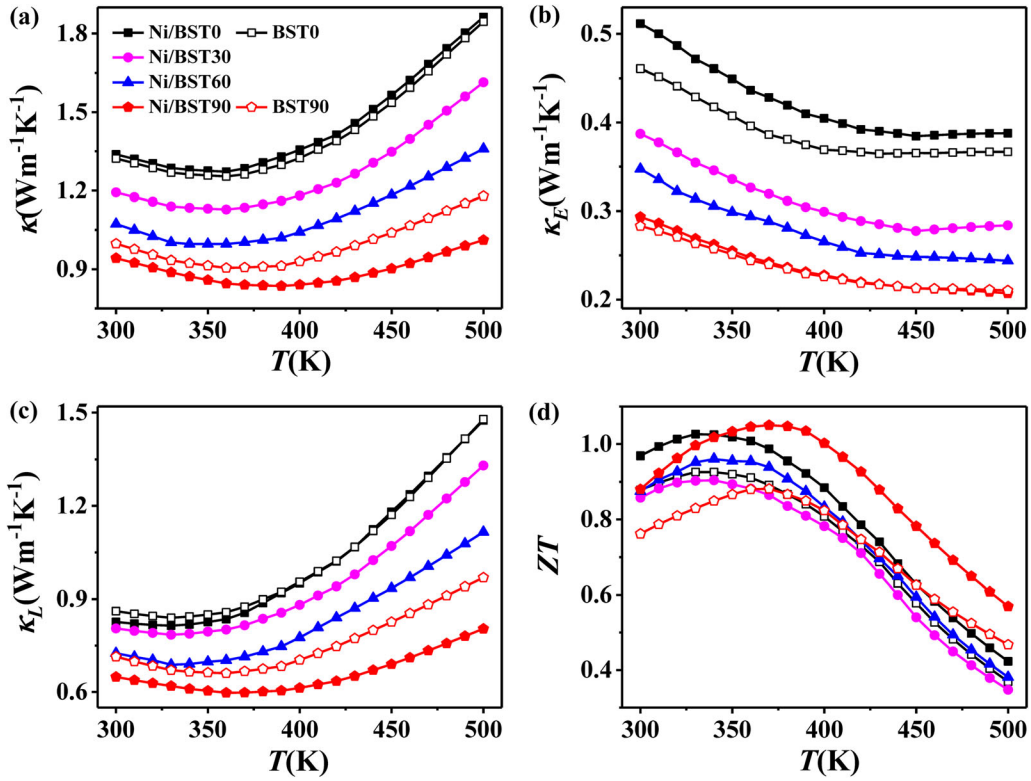

Fig. 6. Temperature dependence of (a) thermal conductivity, (b) electronic thermal conductivity, (c) lattice thermal conductivity and (d) *ZT* values for the Ni/BST heterogeneous multilayered TE materials with different angles.

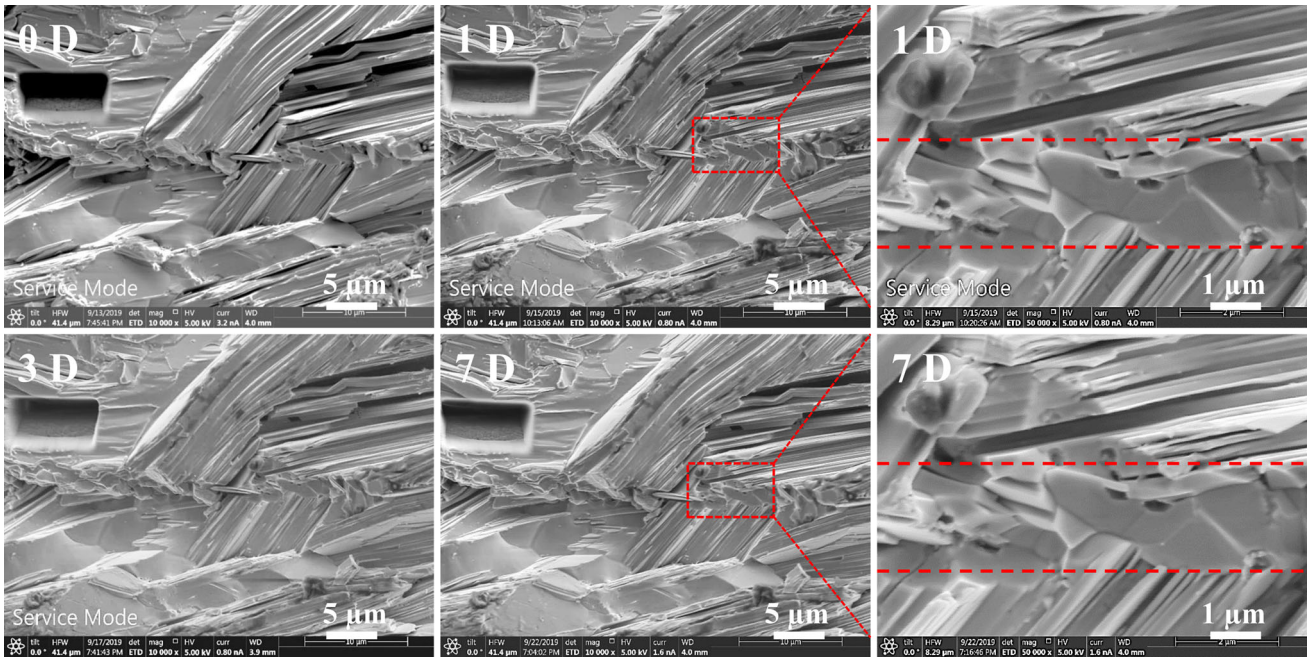

Fig. 7. Cross-sectional morphology of the Ni/BST heterogeneous multilayered TE materials with different annealing time.

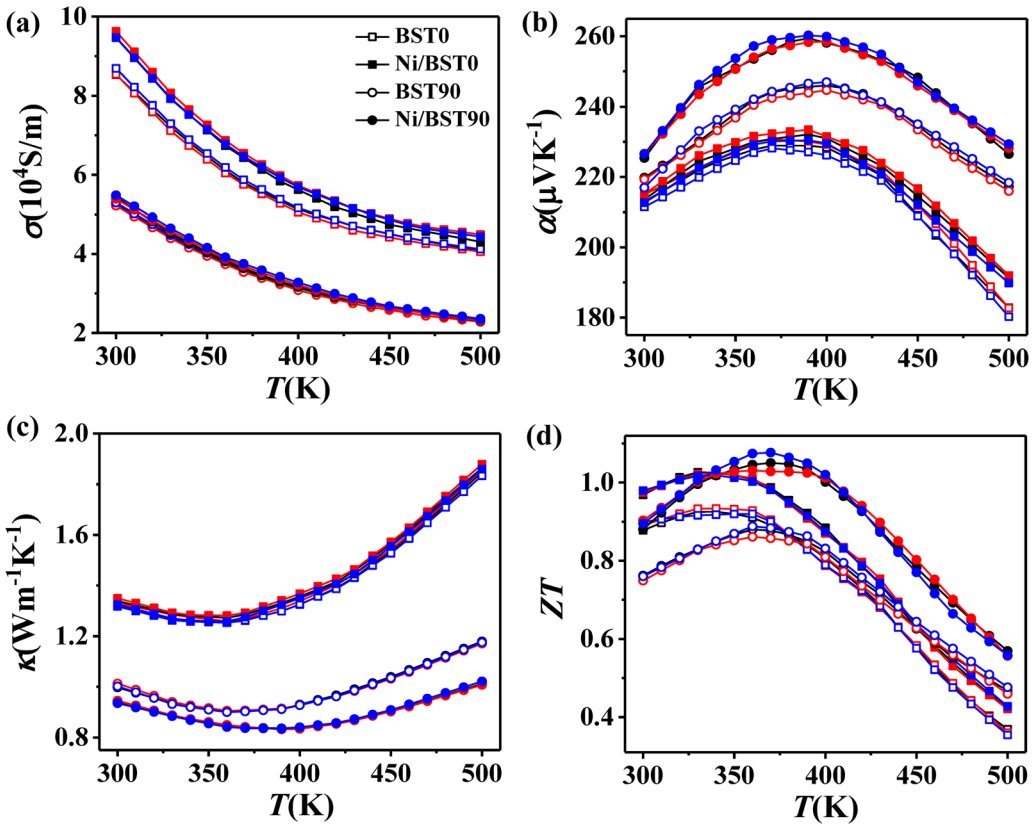

Fig. 8. Temperature dependence of (a) electrical conductivity, (b) seebeck coefficient, (c) thermal conductivity and (d) *ZT* values for the Ni/BST heterogeneous multilayered TE materials in the 0° and 90° angles.

As shown in Fig. 6d, the trend of *ZT* value of all samples increases first and then decreases rapidly with increasing temperature, which is attributed the intrinsic excitation of material. Affected by material anisotropy, the *ZT* value of Ni/BST heterogeneous multilayered TE materials first decreases and then increases with the increase of angle. The *ZT* value of Ni/BST0° increased by 10.7% compared with the BST0° matrix, which is attributed to the large increase in σ. The *ZT* value of Ni/BST90° increases by 19.1% compared with the BST90° and achieves a maximum value of 1.05 at 370 K because of the enhancement of scattering of carriers and phonons caused by heterogeneous interfaces, enhancing the α and reducing the κ simultaneously. Therefore, the introduction of the ordered heterogeneous interfaces in the BST matrix can simultaneously optimize its electrical and thermal transport properties, ultimately resulting in an improvement of the *ZT* value.

To investigate the stability of the interfacial reaction layer, we first use a focused ion beam (FIB, FEI Helios NanoLab G3 UC) to mark the interface area of the sample and characterize its interface morphology. Then, the marked sample was annealed at 473 K in an open tube furnace (KeJing, OTF-1200X) with argon atmosphere for 1 day, 3 days and 7 days, respectively. Finally, the interface morphology of the marked position was characterized by FIB, and the results are shown is Fig. 7. It can be seen that the interface morphology does not change significantly with the increase of annealing time, and the interface is closely bonded, which indicates that the interfacial reaction layer composed of Ni and Te has a good stability.

To verify the repeatability of sample, the TE performance of the samples in the 0° and 90° angles were repeatedly measured three times (represented by black, red and blue lines, respectively) in the range 300–500 K, and the results are shown in Fig. 8. It can be seen that the deviations are very small and within the measurement uncertainties (about $\pm$ 5%), indicating the good repeatability. Therefore, we can conclude that the TE performance of BST can be effectively improved by introducing ordered heterogeneous interfaces.

CONCLUSIONS

A series of Ni/BST heterogeneous multilayered TE materials with different angles (0°, 30°, 60° and 90°, the angles between the performance measurement direction and the Ni layer) were prepared by vacuum evaporation deposition combined with SPS. EPMA and FESEM analyses indicate that distinct heterogeneous interfaces are firmly bonded and the interfacial reaction layer is composed of Ni and Te. The results show that the *PF* of both Ni/BST0° and Ni/BST90° increases compared with the corresponding matrix, which results from the increase of σ and α, respectively, and they are all closely related to the formed heterogeneous interfaces. κ of Ni/BST90° decreases drastically because of the enhancement of phonon scattering related to the formed heterogeneous interfaces. In particular, due to the simultaneous optimization of electrical and thermal transport properties in the Ni/BST90° sample, the maximum *ZT* value of 1.05 is achieved at 370 K, which is 19.1% higher than that of the BST90° matrix. In addition, the stability of the interfacial reaction layer and the repeatability of the sample performance are also well confirmed. This work indicates that the TE performance of $Bi_{0.5}Sb_{1.5}Te_3$ can be effectively improved by introducing the ordered Ni/BST heterogeneous interfaces.

ACKNOWLEDGMENTS

This work was supported by the National Natural Science Foundation of China (Grant Nos. 11834012, 51620105014, 51572210, 51521001) and the National Key R&D Program of China (Grant No. 2018YFB0703603).

CONFLICT OF INTEREST

The authors declared that they have no conflicts of interest.

REFERENCES

1. L.E. Bell, *Science* 321, 1457–1461 (2008).
2. F.J. Disalvo, *Science* 285, 703–706 (1999).
3. S. Sharma, V.K. Dwivedi, and S.N. Pandit, *Int. J. Green Energy* 11, 899–909 (2014).
4. M. Jonson and G.D. Mahan, *Phy. Rev. B* 21, 4223–4229 (1980).
5. Z. Chen, X. Zhang, and Y. Pei, *Adv. Mater.* 30, 1–16 (2018).
6. J.P. Heremans, *Nat. Phys.* 11, 990–991 (2015).
7. S. Lee, K. Esfarjani, T. Luo, J. Zhou, Z. Tian, and G. Chen, *Nat. Commun.* 5, 1–8 (2014).
8. K. Biswas, J. He, I.D. Blum, C.I. Wu, T.P. Hogan, D.N. Seidman, V.P. Dravid, and M.G. Kanatzidis, *Nature* 489, 414–418 (2012).
9. Y. Pei, X. Shi, A. Lalonde, H. Wang, L. Chen, and G.J. Snyder, *Nature* 473, 66–69 (2011).
10. Y. Pei, H. Wang, and G.J. Snyder, *Adv. Mater.* 24, 6125–6135 (2012).
11. L.D. Zhao, G. Tan, S. Hao, J. He, Y. Pei, H. Chi, H. Wang, S. Gong, H. Xu, V.P. Dravid, C. Uher, G.J. Snyder, C. Wolverton, and M.G. Kanatzidis, *Science* 351, 141–144 (2016).
12. W. Zhao, P. Wei, Q. Zhang, C. Dong, L. Liu, and X. Tang, *J. Am. Chem. Soc.* 131, 3713–3720 (2009).
13. W. Zhao, Z. Liu, Z. Sun, Q. Zhang, P. Wei, X. Mu, H. Zhou, C. Li, S. Ma, D. He, P. Ji, W. Zhu, X. Nie, X. Su, X. Tang, B. Shen, X. Dong, J. Yang, Y. Liu, and J. Shi, *Nature* 549, 247–251 (2017).
14. T. Zhu, Y. Liu, C. Fu, J.P. Heremans, J.G. Snyder, and X. Zhao, *Adv. Mater.* 29, 1–26 (2017).
15. S. Nakajima, *J. Phys. Chem. Solids* 24, 479–485 (1962).
16. M.C.T. Caillat, P. Pierrat, H. Scherrer, and S. Scherrer, *J. Phys. Chem. Solids* 53, 1121–1129 (1992).
17. J.J. Shen, L.P. Hu, T.J. Zhu, and X.B. Zhao, *Appl. Phys. Lett.* 99, 1–3 (2011).
18. W. Xie, J. He, S. Zhu, T. Holgate, S. Wang, X. Tang, Q. Zhang, and T.M. Tritt, *J. Mater. Res.* 26, 1791–1799 (2011).
19. D. Liu, X. Li, P.M. Borlido, S. Botti, R. Schmechel, and M. Rettenmayr, *Sci. Rep.* 7, 1–13 (2017).
20. P.J. Taylor, J.R. Maddux, W.A. Jesser, and F.D. Rosi, *J. Appl. Phys.* 85, 7807–7813 (1999).

21. D. Li, X.Y. Qin, J. Zhang, C.J. Song, Y.F. Liu, L. Wang, H.X. Xin, and Z.M. Wang, *RSC Advances* 5, 43717–43722 (2015).
22. D. Kenfaui, B. Lenoir, D. Chateigner, B. Ouladdiaf, M. Gomina, and J.G. Noudem, *J. Eur. Ceram. Soc.* 32, 2405–2414 (2012).
23. D.L. Medlin and G.J. Snyder, *Curr. Opin. Colloid Interface Sci.* 14, 226–235 (2009).
24. Y. Yang, S.H. Xie, F.Y. Ma, and J.Y. Li, *J. Appl. Phys.* 111, 1–7 (2012).
25. S. Li, X. Liu, Y. Liu, F. Liu, J. Luo, and F. Pan, *Nano Energy* 39, 297–305 (2017).
26. Y.C. Tseng, H. Lee, N.Y. Hau, S.P. Feng, and C.M. Chen, *J. Electron. Mater.* 47, 27–34 (2017).
27. W. Liu, H. Wang, L. Wang, X. Wang, G. Joshi, G. Chen, and Z. Ren, *J. Mater. Chem. A* 1, 13093–13100 (2013).
28. W.P. Lin, D.E. Wesolowski, and C.C. Lee, *J. Mater. Sci.: Mater. Electron.* 22, 1313–1320 (2011).
29. W.H. Chao, Y.R. Chen, S.C. Tseng, P.H. Yang, R.J. Wu, and J.Y. Hwang, *Thin Solid Films* 570, 172–177 (2014).
30. Y.C. Lan, D.Z. Wang, G. Chen, and Z.F. Ren, *Appl. Phys. Lett.* 92, 1–3 (2008).
31. Y.P. Yadava and R.A. Singh, *J. Mater. Sci. Lett.* 4, 1421–1424 (1985).
32. R.A. Howe, J.E. Enderby, and R.J. Newport, *J. Phys. C: Solid State Phys.* 15, 4635–4640 (1981).
33. T.A. By, R.J. Bither, W.H. Bouchard, P. Cloud, C. Dokohue, and A.W.J. Siemoks, *Inorg. Chem.* 7, 2208–2220 (1968).
34. H.S. Kim, Z.M. Gibbs, Y. Tang, H. Wang, and G.J. Snyder, *APL Materials* 3, 1–5 (2015).
35. X. Mu, H.Y. Zhou, D.Q. He, W.Y. Zhao, P. Wei, W.T. Zhu, X.L. Nie, H.J. Liu, and Q.J. Zhang, *Nano Energy* 33, 55–64 (2017).